Chem

CellPress

Article

Programmable ATP-Fueled DNA Coacervates by Transient Liquid-Liquid Phase Separation

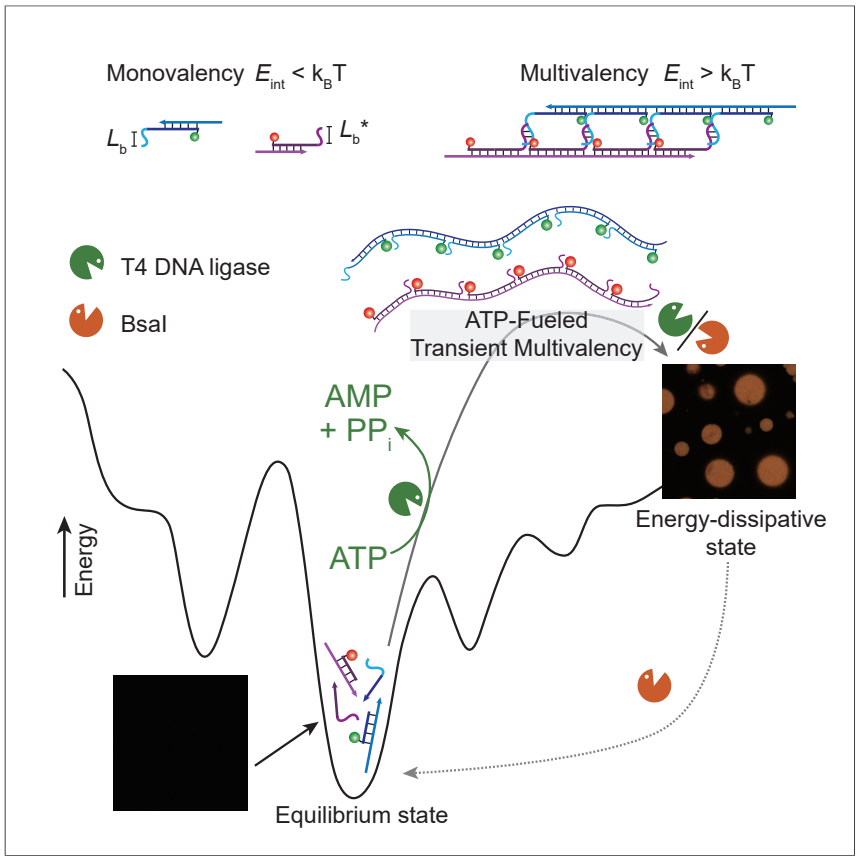

This study demonstrates transient, multivalency-driven liquid-liquid phase separation (LLPS) of sequence-defined functionalized nucleic acid polymers to prepare functional all-DNA coacervates. The coacervates need ATP as a fuel to drive their formation and disappear once the ATP is consumed in a fuel-driven process—an autonomous system with tunable lifetime. The programmable nature of the DNA system allows to run sorted LLPS of two different species in parallel for multicomponent coacervates and can be used to entrap bioactive species to generate functions.

Jie Deng, Andreas Walther

andreas.walther@uni-mainz.de

HIGHLIGHTS

Programmable multivalency to trigger liquid-liquid phase separation and coacervation

Autonomous coacervates with tunable lifetimes by ATP concentration

Self-sorting coacervates by orthogonal multivalent recognitions

Entrapment of secondary species and enzyme cascades to generate versatile functions

Deng & Walther, Chem 6, 3329–3343
December 3, 2020
https://doi.org/10.1016/j.chempr.2020.09.022

Chem

CellPress

Article

Programmable ATP-Fueled DNA Coacervates by Transient Liquid-Liquid Phase Separation

Jie Deng[1,3,4] and Andreas Walther[1,2,3,4,5,6,*]

SUMMARY

Multivalency-driven liquid-liquid phase separation (LLPS) is essential for biomolecular condensates to facilitate spatiotemporal regulation of biological functions. Providing programmable model systems would help to better understand the LLPS processes in biology and furnish new types of compartmentalized synthetic reaction crucibles that exploit biological principles. Herein, we demonstrate a concept for programming LLPS using transient multivalency between ATP-driven sequence-defined functionalized nucleic acid polymers (SfNAPs), which serve as simple models for membrane-less organelles. Critically, the prominent programmability of the DNA-based building blocks allows to encode distinct molecular recognitions for multiple multivalent systems, enabling sorted LLPS and, thus, multicomponent DNA coacervates. The ATP-driven coacervates are capable for multivalent trapping of micron-scale colloids and biomolecules to generate functions as emphasized for rate enhancements in enzymatic cascades. This work demonstrates ATP-driven multivalent coacervation as a valuable mechanism for dynamic multicomponent and functional biomolecular condensate mimics and for autonomous materials design in general.

INTRODUCTION

Membrane-less biomolecular condensates are ubiquitous in biological cells and are important for spatiotemporal organization of subcellular processes.[1–3] These biomolecular condensates function to concentrate proteins and nucleic acids and provide diverse biological functions, such as RNA metabolism, ribosome biogenesis, and signal transduction.[2,4–6] Many of them show liquid-like properties, such as rapid condensation and dissolution, fusion, and wetting.[7,8] For instance, the nucleoli, Cajal bodies, and nuclear speckles in the nucleus can vary their size, number, and composition over time and can reversibly appear and disappear during mitosis.[9,10] Although all mechanisms for the dynamic changes remain elusive, multivalent interactions between the (bio)macromolecular components are a key driving principle in their dynamic regulations.[6,11–13] Inspired by this natural multivalency-driven liquid-liquid phase separation (LLPS), biomolecular recognition units have, for instance, been encoded into pairs of engineered proteins, which then show the capability for phase transition upon mixing, leading to micrometer-sized liquid droplets.[6]

Aside from biomolecular recognition, numerous strategies, such as charge-charge, dipole-dipole, cation-π, and π-π interactions, have been developed to construct related, in parts fully synthetic, coacervates and complex coacervates.[14–18] Recently, such coacervates have regained interest as artificial membrane-less organelles,

The Bigger Picture

Multivalency-driven liquid-liquid phase separation (LLPS) is essential for functional membrane-less organelles, and multicomponent organelles forming via orthogonal multivalent recognitions are ubiquitous in biological systems. Although much progress has been made in artificial membrane-less organelles, highly programmable LLPS and concepts, such as programmable recognition, are missing and hinder the development of rational and tunable artificial organelles for the design of functions. Additionally, the understanding of the dynamic formation mechanisms in membrane-less organelles is still poor. In this work, we report a generic model system for membrane-less organelles based on programmable multivalency-driven LLPS of dynamic DNA polymers, as orchestrated by ATP-driven non-equilibrium reaction networks. The system benefits from its outstanding tunability and versatility and paves the way for dynamic multicomponent artificial organelles with diverse functions.

which could act as open reactors with facile exchanges of matter.[19–22] Specifically, polyelectrolyte complexation is intriguing for facile and versatile coacervate fabrication. Examples include carboxymethyl dextran sodium salt/poly-L-lysine (PLL),[20] oppositely charged amylose derivatives,[23] ATP-poly(diallyldimethyl ammonium chloride),[24] ATP/PLL,[25] and others.[26–31] The unstable membrane-less coacervates can be stabilized by interfacial self-assembly of synthetic surfactants and stoichiometry mismatch of the charges.[23]

To allow external control mechanisms, various chemical signals and physical stimuli have been used to reversibly assemble polyelectrolyte-based coacervates.[25,32–35] Mann and co-workers reported reversible coacervation via alternately bubbling CO_2 and NH_3 to ATP/PLL coacervates to regulate the PLL charge.[36] Keating and co-workers investigated the switching of RNA-peptide coacervates by changing the peptide phosphorylation state using a kinase-phosphatase pair.[37] Moreover, ATP/PLL coacervates were coupled to an enzymatic reaction network (ERN) that transiently generates ATP as one component of the coacervate.[38] Toward active matter coacervates, Huck and co-workers reported a GTP-driven polymerization of FtsZ protein within coacervates for dynamic coacervate deformation and fission.[39] In summary, although great progress has been made in coacervates as mimics for membrane-less organelles and for protocell research, most coacervates rely on polyelectrolyte interactions, whereas highly programmable molecular recognition for the formation of LLPS has scarcely been addressed.[6] Such highly programmable interactions would, however, contribute fundamentally relevant model systems to quantitatively understand kinetics and thermodynamics of LLPS, provide means to modulate the dynamics and selective uptake, and, if orthogonal interactions were available, also help in the preparation of spatially sorted dynamic artificial membrane-less organelles. Additionally, the emerging concepts of non-equilibrium chemically fueled systems empowered by chemical reaction networks can contribute new features, such as transience and programmable dynamics.[40–42]

In the DNA nanoscience arena, droplets made of DNA could feature outstanding programmability and molecular recognition.[43–46] In terms of DNA droplets, DNA nanostars have been investigated for controllable liquid properties and macromolecular structures.[47–49] Moreover, Mao and co-workers reported all-DNA droplets by condensation of palindromic domains in single-stranded DNA (ssDNA),[50] which, however, showed ill-defined structures. We previously reported pathway-controlled formation of membrane-less all-DNA droplets with well-defined structures using temperature-induced LLPS of poly(adenine)-rich ssDNA strands and subsequent kinetic trapping of the coacervates during cooling—again using palindromic domains.[51] Both strategies need high temperature annealing to form the droplets, which is incompatible with applications in a biological system, involving, for instance, the encapsulation of enzymes or other temperature-sensitive components. Although first DNA temperature-annealing derived droplets exist, exploiting distinct molecular recognition for constructing multicomponent DNA-based droplets is uncharted territory, and the potential of DNA for regulating dynamics (e.g., reversible condensation and dissociation, and transient coacervation) and for realizing isothermal LLPS to open possibilities to encapsulate temperature-sensitive components, such as enzymes or proteins in general, has not been addressed.

Herein, we report ATP-driven membrane-less all-DNA coacervates, which form through multivalency-driven LLPS of programmable sequence-defined functionalized nucleic acid polymers (SfNAPs) orchestrated by an ERN of concurrent ATP-powered ligation (using T4 DNA ligase) and endonuclease-controlled

[1]Institute for Macromolecular Chemistry, University of Freiburg, Stefan-Meier-Straße 31, 79104 Freiburg, Germany

[2]DFG Cluster of Excellence "Living, Adaptive and Energy-Autonomous Materials Systems" (livMatS), 79110 Freiburg, Germany

[3]Freiburg Materials Research Center, University of Freiburg, Stefan-Meier-Straße 21, 79104 Freiburg, Germany

[4]Freiburg Center for Interactive Materials and Bioinspired Technologies (FIT), University of Freiburg, Georges-Köhler-Allee 105, 79110 Freiburg, Germany

[5]Lead Contact

[6]Present address: A3BMS Lab, Department of Chemistry, University of Mainz, Duesbergweg 10-14, 55128 Mainz, Germany.

*Correspondence: andreas.walther@uni-mainz.de

https://doi.org/10.1016/j.chempr.2020.09.022

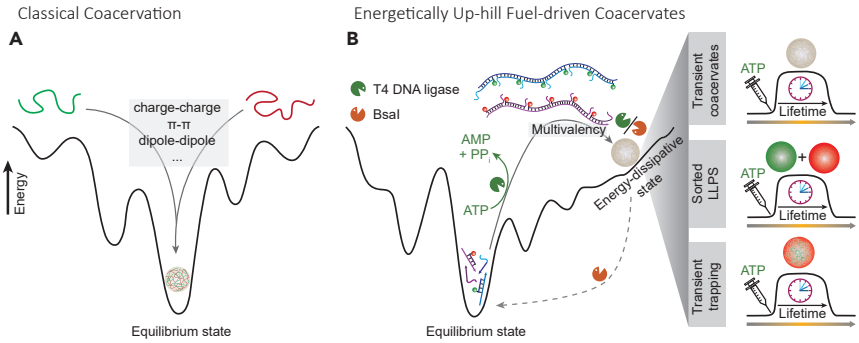

Figure 1. ATP-Driven LLPS by Programmable Interactions in Multivalent SfNAPs with Complementary Side-Chain Interactions

(A) Schematic illustration of the energy landscape for classical coacervation processes.

(B) ATP-driven transient SfNAPs to engineer transient all-DNA coacervates, sorted LLPS coacervates system, and transient trapping of secondary components. The dynamic coacervate structures sit at an energy-dissipative state out of the global minimum in the energy landscape. Transient lifetimes occur because the ATP fuel is consumed as detailed in the ERN in Figure 3A.

restriction (using BsaI). Using orthogonally polymerizing SfNAPs system (due to distinct molecular recognition in the main chain of various building blocks), we further demonstrate the self-sorting of LLPS for multicomponent coacervates in the same system. To showcase functions of the coacervates, we reveal transient entrapment and release of functionalized micron-scale colloids and functional DNA polymers within the ATP-driven all-DNA coacervates. Additionally, glucose oxidase (GOx) and horseradish peroxidase (HPR) fusion proteins bound to streptavidin can be encapsulated in the coacervates by anchoring onto biotinylated coacervate-forming SfNAPs. An improved catalytic activity of the GOx/HPR enzyme cascade is found within the membrane-less compartments with a macromolecularly crowded DNA environment.

RESULTS

General Concept for ATP-Driven Molecular Recognition and Multicomponent All-DNA Coacervates

We first highlight the differences in free energy between classical coacervates and chemically fueled coacervates. Classical coacervation based on attractive interactions between two polymers occurs in an energetically down-hill process by formation of enthalpic interactions and entropically favored release of water (and counterions for polyelectrolytes).[18] The resulting coacervate droplets sit near the global minimum in the energy landscape (Figure 1A). In our design, we implemented an ATP-fueled system to obtain the coacervates in a dynamic and energy-dissipative state (Figure 1B). It builds on our recently introduced systems of ATP-driven transient DNA polymerization and SfNAPs with transient generation of multivalent interactions with colloid objects.[52–54] We hypothesized that two SfNAPs with complementary side-chain interactions could allow establishment of membrane-less coacervates by LLPS, providing a programmable mimicry of biomolecular condensates driven by multivalency. The injection of ATP to a system containing small building blocks with complementary sticky ends and the enzymes (T4 DNA ligase and BsaI restriction enzyme) allows to drive the system isothermally into a dynamic steady state (DySS) with temporal SfNAP formation. More details on the ERN are below in Figure 3A. The ATP is consumed in the process, and the energy is transiently transferred into DNA phosphodiester bonds, resulting in a fuel-driven dynamic covalent bond with an average steady-state chain length. Under the conditions of the ERN, the

phosphodiester bond is unstable (ΔG = −5.3 kcal/mol[55]). Constant ATP-dissipating bond shuffling occurs in the energy-driven steady state. The forward and backward reactions are not each other's inverse and are separate kinetically tunable reactions. The network is reminiscent of non-equilibrium steady-state phosphorylation-dephosphorylation networks without any outside regulator.[56–60] This qualifies the system as a chemically fueled non-equilibrium system, in which the ATP concentration majorly sets the lifetime, and the antagonistic enzymes engineer the transduction kinetics and dynamics of the system.[52]

Since the side chains on the SfNAPs are independent from the ERN, they are freely programmable with regard to their sequences, and thus, hybridization strength. Additionally, since BsaI is a class IIS endonuclease with separated domains for recognition and restriction, a careful selection of the ligation parts for the main chain and of the side chain interaction sites on various DNA building blocks allows running multiple coacervating systems in parallel and achieving sorted LLPS and multicomponent coacervates. 4 nucleotides (nt) of the sticky end overhangs at the restriction site can be freely programmed in BsaI, enabling in principle 4^4 = 256 orthogonal interactions in multicomponent systems. Importantly, the multivalency-driven coacervates are able to trap multivalent binder-functionalized objects, such as micron-scale colloids and catalytic enzymes (Figure 1).

Multivalency-Guided LLPS of Complementary SfNAPs for Membrane-less All-DNA Coacervates

For proof-of-concept, we discuss the static multivalency-guided LLPS of two SfNAPs with complementary side chains before discussing the dynamic ATP-fueled transient systems. Under appropriate enthalpic balance, efficient cooperative multivalent binding between the side chains of two SfNAPs occurs only in the polymer state, whereas binding is absent in the monomer state. This is a function of the interaction length of the complementary part (L_b) and the distance between the side chains (d_b; Figure 2A). Based on preliminary screening, we found that a L_b of 8 base pairs (bp; CGAATAGA/TCTATTCG (T_m = 33°C) requires a d_b of ca. 38 bp or smaller to realize efficient multivalency in the ATP-driven SfNAP state. These conditions set the starting point here. We synthesized two orthogonal SfNAPs, SfNAP1 and SfNAP2, by separate ligation of M1/M2 and M3/M4, whereby M2 and M4 carry the side chains with complementary interactions (Figure 2B, sequences in Table S1). $ATTO_{488}$ and $ATTO_{647}$ dyes in M1 and M3 fluorescently label both SfNAPs for confocal laser scanning microscopy (CLSM). Agarose gel electrophoresis (AGE) yields polymer length distributions of the SfNAPs with a growth up to 1,500 bps (Figure 2C).

Afterward, we investigated the coacervation of SfNAP1 and SfNAP2 (10 μM for each species regarding amounts of repeating units) by mixing and shaking using an orbital shaker at 80 revolutions per minute (rpm) at 37°C. CLSM in Figure 2E indeed confirms the formation of spherical all-DNA coacervates. After 30 min, DNA coacervates with a number average diameter (D_n) of ca. 5.2 μm were formed, and the D_n increases to ca. 10.5 μm at 1 h, reaching a balanced state for LLPS at ca. 1 h. Both fluorophores are homogeneously distributed in the coacervates confirming intimate mixing of the SfNAPs (Figure 2E). Note that control experiments of monomer mixtures or the individual SfNAPs do not give any structure in CLSM, because the multivalent interactions are absent. Herein, we realize LLPS for membrane-less coacervates in a non-protein-based synthetic system via DNA-based multivalent interaction.

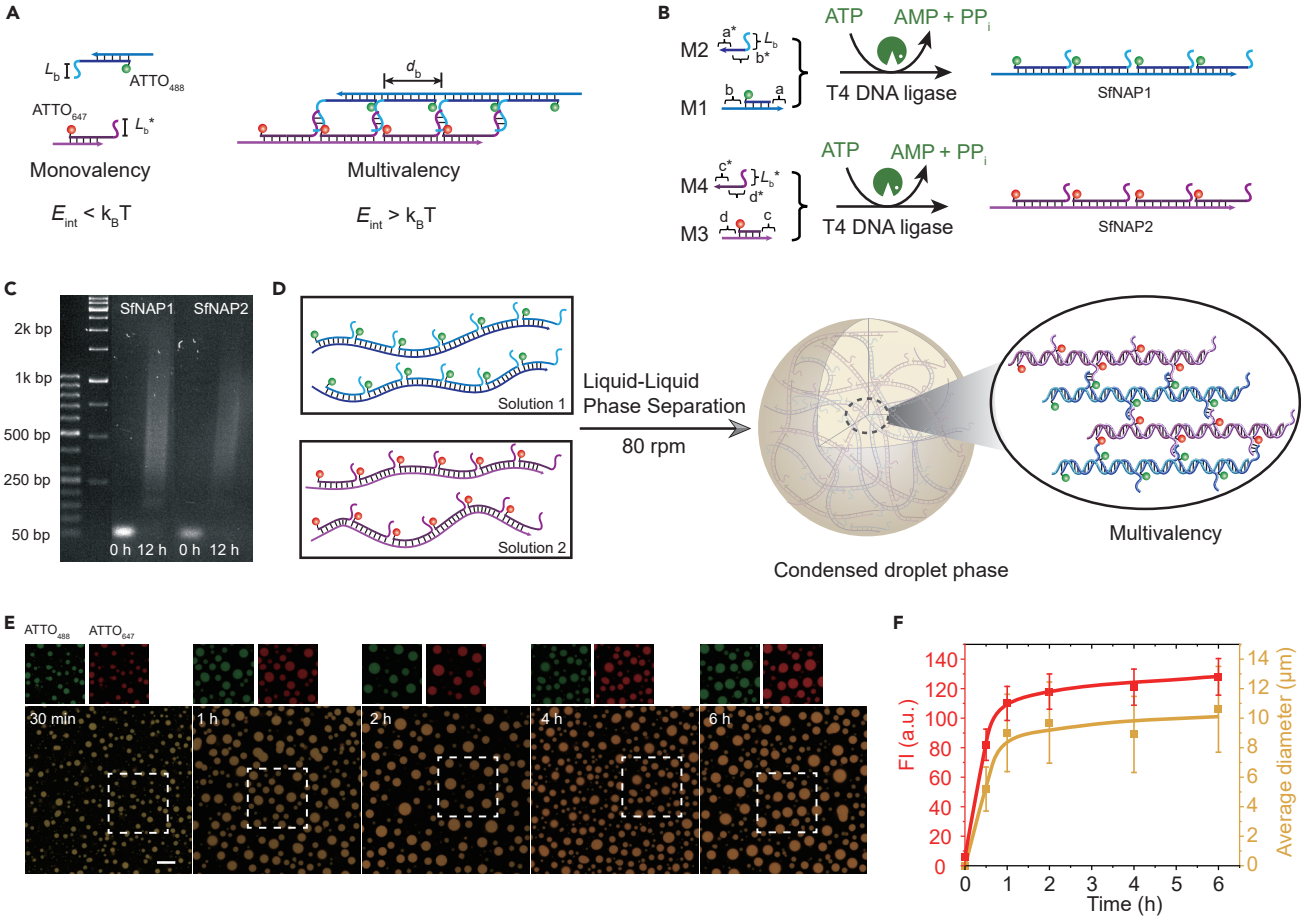

Figure 2. Multivalency-Driven LLPS for Membrane-Less All-DNA Coacervates

(A) Monovalent versus multivalent binding with programmable interaction strength, L_b, and branch distance, d_b.

(B) Schematic illustration of ATP-driven multiple SfNAPs.

(C) AGE for the polymerizations at start and end (12 h; 2 wt %, 90 V, 2 h).

(D) Schematic illustration of multivalency-guided LLPS of two SfNAPs with complementary side-chain interactions for all-DNA coacervate formation.

(E) Time-dependent CLSM of DNA coacervates. Scale bar, 20 μm.

(F) Time-dependent fluorescence intensities of $ATTO_{647}$ and average diameters for the coacervates. Error bars are standard deviations from three random fields of view of duplicate experiments (ca. 300 coacervates). Lines are guides to the eye.

ATP-Driven Transient All-DNA Coacervates with Programmable Lifetimes

In the above investigation, the distinct difference between LLPS for the mixed SfNAPs and absence of LLPS for the monomer tiles is the key to regulate the temporal behavior of the all-DNA coacervates. To realize an energy-dissipative coacervation system, we combined the SfNAPs with the full ERN featuring concurrent ligation/polymerization and restriction/depolymerization (Figures 3A and 3B). Typical experiments were conducted using ca. 0.01 mM of each DNA tile (M1-M4), 0.92 WU/μL T4 DNA ligase, 1.0 U/μL BsaI, and varied ATP concentrations at 37°C. CLSM measurements at different time points reveal the transient nature of the ATP-driven all-DNA coacervates regarding their structural evolution (Figures 3C and S1). Before ATP injection, the system is a fully homogeneous solution. The injection of 0.06 mM ATP drives the multicomponent system into the SfNAP state with dynamic sub-unit exchange, and the build-up of the multivalency between the SfNAPs induces LLPS (Figures 3C–3I). After 30 min, some small DNA coacervates with a $D_n \approx 1$ μm are observed under CLSM, for which the fluorescence intensity (FI)

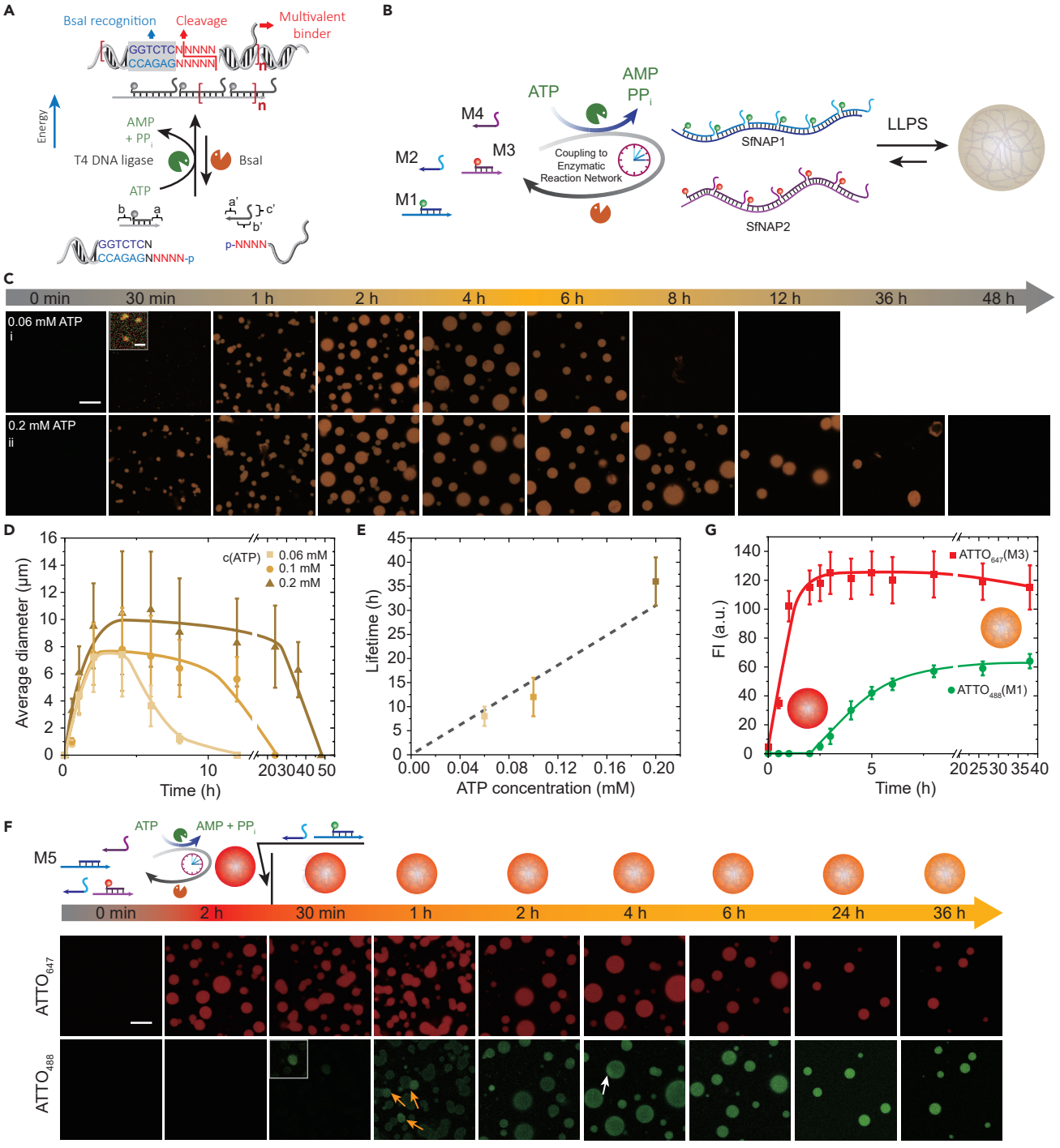

Figure 3. ATP-Driven Transient All-DNA Coacervates with Programmable Lifetimes

(A) Schematic illustration of the ERN furnishing an ATP-driven transient SfNAP.

(B) Schematic illustration of ATP-driven membrane-less all-DNA coacervates via LLPS driven by transient multivalency of orthogonal SfNAPs.

(C) Time-dependent CLSM measurements for transient all-DNA coacervates with programmable lifetimes by fueling with varied concentration of ATP (0.06 and 0.2 mM). CLSM measurements were conducted consecutively with the same microscopy settings. Scale bar, 20 μm; insert = 2 μm.

(D) Time-dependent size of the transient coacervates with programmable lifetimes. Error bars are standard deviations from three random fields of view of duplicate experiments. Lines are guides to the eye.

(E) Lifetimes are controlled by the ATP concentrations. Error bars are standard deviations of duplicate measurements. Line is a guide to the eye.

Figure 3. *Continued*

(F) Tile integration and dynamization during a running transient coacervates system. The tile with $ATTO_{488}$ was added 2 h after starting the initial system. CLSM before and after adding the $ATTO_{488}$ tile confirm the integration and reconfiguration. Scale bar, 20 μm.

(G) Time-dependent fluorescence intensities. Error bars are standard deviations from three random fields of view of duplicate experiments. Lines are guides to the eye. Conditions for (B) 37°C, 0.01 mM M1, 0.012 mM M2, 0.01 mM M3, 0.012 mM M4, 0.92 WU/μL T4 DNA ligase, 1.0 U/μL BsaI, and varying amounts of ATP, under orbital shaking at 80 rpm. Conditions for (F) 37°C, 0.01 mM M5, 0.012 mM M2, 0.01 mM M3, 0.012 mM M4, 0.92 WU/μL T4 DNA ligase, 1.0 U/μL BsaI, and 0.2 mM of ATP, under orbital shaking at 80 rpm, followed by addition of another 0.002 mM M1 and 0.0024 mM M2 after 2-h running of the transient coacervation reaction.

is very weak. Subsequently, further growth occurs and a relatively steady plateau with a $D_n \approx 7$ μm is reached after ca. 2 h (Figure 3D). Concurrently, the averaged fluorescence intensities for the coacervates also drastically increase to a DySS (Figure S2). The constant D_n in the plateau is obtained because of slight orbital shaking to mitigate coalescence. After the ATP is consumed, the DNA coacervates disappear, because the long SfNAPs are degraded back to monomeric building blocks by BsaI. The coacervate lifetime is tunable from 6 h to 1.5 days by changing the ATP concentration from 0.06 to 0.2 mM (Figure 3E), which indicates the tiles produced after endonuclease restriction continue to be active and recycled in the ERN. The kinetics of coacervate formation and the coacervate size increase mildly with the ATP concentration, which is due to a faster polymerization process as ATP is a co-factor in the ligation and provides ionic strength to promote DNA interactions (Figures 3Cii, 3d, and S1). AGE analyses of the transient SfNAPs in these systems confirms similar lifetimes for the molecular and coacervate levels. Higher ATP concentrations indeed lead to faster polymerization of transient SfNAPs to promote the kinetics for LLPS (Figure S3). Interestingly, selected coacervates degrade from the inside and end up being hollow capsules during the degradation. This confirms the entrapment and operation of the enzymes inside the coacervates (Figure S1). Additionally, in the DySS (when the system is still rich in ATP), no capsule formation is observed. This indicates that in the coacervates the kinetic for ligation is faster than restriction to maintain the structure. Consequently, the polymers can still be dynamically extended when in the coacervate phase if excess ATP and ligation overhangs are present.

It is also worth noting that orbital shaking is crucial for controlling the dynamic property of the coacervates. Without any shaking, the coacervates sediment and merge together to form random aggregates (Figure S4D), while strong shaking (e.g., at 400 rpm) leads to smaller coacervates with D_n from several hundred nanometers to ca. 1 μm (Figures S4B and S4C). This demonstrates that fusion and fission occur during shaking as a dynamic system feature. We also characterized the liquid property of fully suspended coacervates by real-time fusion experiments. Upon contacting, two coacervates merge into one large coacervate, which verifies the liquid-like nature of the DNA coacervates (Figure S5; Video S1). The droplets can wet the glass surface (Figure S4D), but after wetting, the droplets cannot be recovered by further shaking. Hence, the orbital shaking can also mitigate the wetting of the droplets on the glass surface.

We further probed the internal dynamics of the coacervates in the ATP-driven steady state to detect the efficiency of component diffusion in the coacervates. We added differently labeled $ATTO_{488}$-M1 monomers to a running system based on non-fluorescent SfNAP1 (M2/M5) and $ATTO_{647}$-labeled SfNAP2 (M3/M4). $ATTO_{488}$-M1 shares the same sequence with M5 to co-integrate with SfNAP1. Before M1 addition, only red fluorescence can be observed, because the coacervates are only labeled by $ATTO_{647}$ on SfNAP2 (Figure 3F). After the addition of $ATTO_{488}$-M1, green $ATTO_{488}$ fluorescence gradually arises in the coacervates (Figure 3F), while the red $ATTO_{647}$ FI

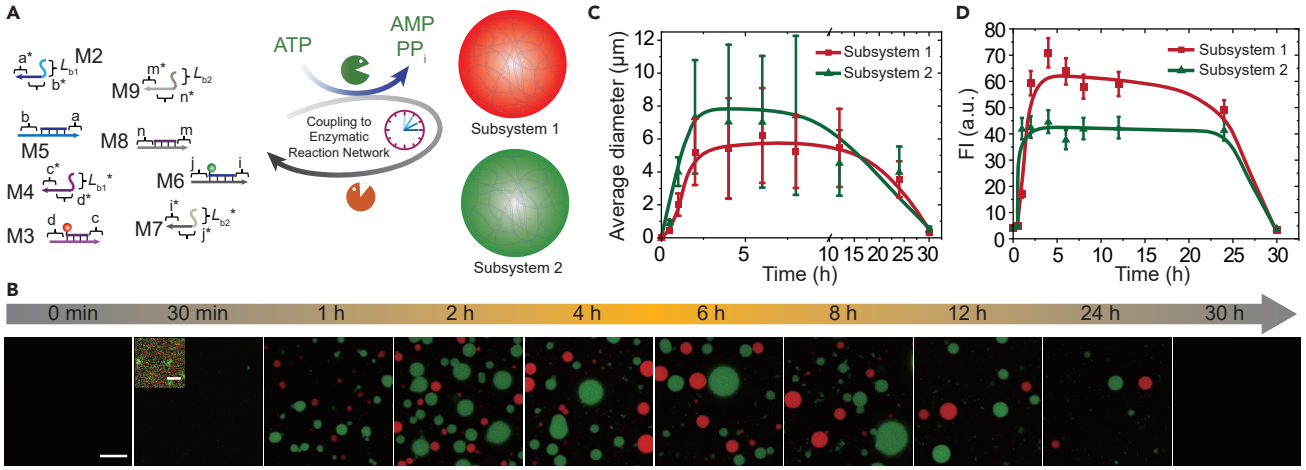

Figure 4. Self-Sorting ATP-Driven Transient Multicomponent Membrane-Less Coacervates

(A) Schematic illustration of ATP-driven multiple coacervation systems. Subsystem one is formed by M2–M5 and subsystem two is formed by M6–M9.

(B) Time-dependent CLSM measurements of the transient multiple coacervates. CLSM measurements were conducted consecutively with the same microscopy settings. Scale bar, 20 μm; insert = 4 μm.

(C) Time-dependent average diameters of the transient coacervates for both systems. Lines are guides to the eye. Error bars are standard deviation from three random fields of view of duplicate experiments.

(D) Time-dependent fluorescence intensities of the transient coacervates for both systems. Error bars are standard deviations from three random fields of view of duplicate experiments. Lines are guides to the eye. Conditions: 37°C, 0.01 mM M5, 0.012 mM M2, 0.01 mM M3, 0.012 mM M4, 0.01 mM M6, 0.012 mM M7, 0.01 mM M8, 0.012 mM M9, 0.92 WU/μL T4 DNA ligase, 1.0 U/μL BsaI, and 0.12 mM ATP, under orbital shaking at 80 rpm.

remains unchanged (Figure 3G). Interestingly, for the first 4 h after the addition of M1, the uptake and distribution of $ATTO_{488}$-M1 to the coacervates is not homogeneous. Coacervates with distinctly brighter fluorescence can be observed at, e.g., 1 h. This is due to slow mixing when adding the $ATTO_{488}$-M1 and preferential uptake. More interestingly, at 4 h, patches of brighter fluorescence can be observed in otherwise spherical coacervates (white arrow). These arise from fusion events (visible, e.g., at 1 h, orange arrows) and subsequent recircularization of the coacervates to minimize interfacial energy (Figure 3F). These patches disappear within 6 h and fully homogeneous coacervates are obtained. This confirms the dynamic chain shuffling inside the coacervates and deep integration of secondary tiles. Such a covalent integration of a new monomer species would be impossible in a static non-driven system, as the DNA bonds would be static. This clearly emphasizes an advantage toward quick structural and functional adaptation due to operating the structures in a DySS with constant bond shuffling.[61]

ATP-Driven Transient Multiple Sorted Membrane-Less Coacervates

The programmability of the ligation-restriction position and of the complementary side chains on the SfNAPs opens the possibility to potentially run multiple LLPS systems in parallel. Figure 4A shows such a design, in which four distinct SfNAPs can be temporarily programmed in the ERN, where two SfNAPs subsets feature orthogonal multivalent interactions (L_{1b}/L_{1b}* and L_{2b}/L_{2b}*) to form self-sorted LLPS. Subsystem 1 consists of M5/M2 and $ATTO_{647}$-M3/M4. Subsystem 2 consists of $ATTO_{488}$-M6/M7 and M8/M9. The fluorescent labels allow for distinguishing the self-sorted LLPS. Time-dependent CLSM indeed confirms orthogonal coacervate formation and the transient nature of both ATP-driven multicomponent coacervates (Figure 4). The transient behavior is analogous to the single-pair coacervates, and spatially resolved fluorescence analysis in the CLSM shows absence of crosstalk. The absence of crosstalk here is attributed to the absence of attractive specific multivalent interactions between different coacervates, that otherwise possess repulsive electrostatic

interactions due to their charged nature. This also confirms that the multivalent interaction among the coacervates from the same species facilitate the fusion of contacting coacervates (Figure S5; Video S1). This demonstrates that ATP-driven sorted LLPS can be achieved by defining molecular recognition events to form the ATP-driven SfNAPs and to guide the multivalent interactions between them. Although collision events happen between the two sorted populations during operation, those do not suffice for a merging and fusion into common droplets. A crosstalk, such as in common polyelectrolyte coacervates, using non-specific interactions can be prevented.[23] Such multicomponent membrane-less coacervates are reminiscent of diverse membrane-less organelles driven by multivalent recognitions in a biological system and are a clear advantage provided by the high programmability of DNA and of our ATP-driven ERN using BsaI as class IIS endonuclease.[2]

Transient Trapping and Releasing for Temporal Superstructures

We surmised that the multivalent recognition patterns driving the LLPS would provide a generic platform to entrap objects functionalized with complementary ssDNA. Figure 5A shows a first example by transiently trapping ssDNA-functionalized micron-sized colloids (D = 1 μm) in the DNA coacervates. For clear visualization, the colloids and coacervates are labeled with $ATTO_{488}$ and $ATTO_{647}$, respectively. Time-dependent CLSM visualizes the transient all-DNA coacervate formation and concurrent colloid aggregation, engulfment, and restructuring. Before ATP injection, the colloids are freely dispersed in the solution (Figure 5C). The addition of ATP drives the formation of two orthogonal SfNAPs with complementary side chain interactions. On the one hand, this leads to LLPS between SfNAP1 and SfNAP2. From above (Figure 2), we know that this process takes up to 30 min to lead to visible structure formation. This is due to the fact that both SfNAPs first need to build up long chains for efficient interaction. On the other hand, the non-fluorescent SfNAP1 (M5 and M2) can interact with the already present multivalent recognition pattern on the colloids. This process is faster (less than 10 min), and hence, colloid assembly happens prior to the formation of any obvious DNA coacervates. After 30 min, clear fractal aggregates of the colloids (reminiscent of diffusion-controlled aggregation) are visible. After 1 h, the coacervates become clearly visible (red fluorescent) and nucleate largely on these structures. Engulfment and encapsulation happen due to the competition of multivalent interactions and the dynamics of the system (Figure 5C). Additionally, the dynamics lead to some level of reorientation from the more fractal aggregation to a more spherical superstructure. Interestingly, in the disassembly phase, after ATP is consumed (4 h), the degradation of the coacervates is much faster than the colloidal disassembly. We attribute this to the lower BsaI accessibility of the SfNPAs between the colloid aggregates. After 6 h, all colloid aggregates largely re-disperse in the solution (Figure 5C). It is worth noting that by using lower concentration of functionalized colloids (10% of the one above), smaller colloid aggregates can be obtained and the fractal aggregation in the initial state is absent (Figure S6). This is due to the fact that lower particle concentrations allow significantly less collisions needed for assembly, and the assembly timescale is more synchronized with the LLPS of both SfNAPs.

Aside from trapping colloids in the coacervates for superstructure formation, we further show the encapsulation of functional polymers inside the coacervates (Figures 5B and 5D–5G). Typical experiments were performed by running the above $ATTO_{647}$-labeled M3/M4-M5/M2 coacervates (red channel) together with a Cy3 and biotin-labeled static Cy3/biotin-SfNAP (green channel) without recognition sequence for BsaI, bearing one of the complementary multivalent binders. The Cy3/biotin-SfNAPs is only present in 0.02 mol % of the coacervate SfNAPs.

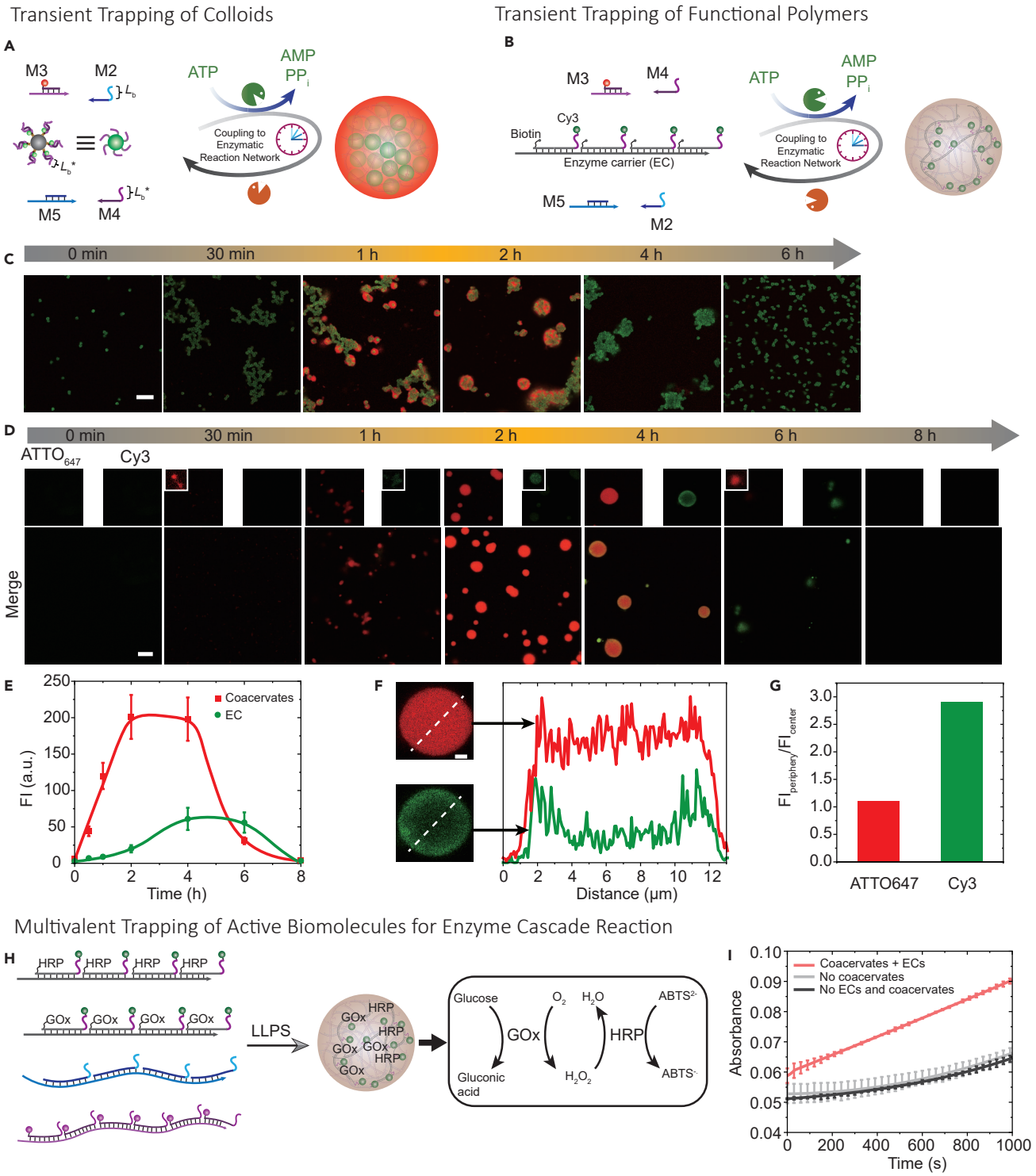

Figure 5. Multivalency-Driven Superstructures and Catalytically Active Coacervates

(A) Schematic illustration of ATP-driven transient coacervates for temporal trapping of micron-sized colloids.

(B) Schematic illustration for ATP-driven transient trapping of functional DNA polymers in the DNA coacervates via multivalency.

(C) Time-dependent CLSM of the transient colloid assembly and transient coacervates. CLSM measurements were conducted consecutively with the same microscopy settings. Scale bar, 10 μm.

Figure 5. *Continued*

(D) Time-dependent CLSM measurements of the transient coacervates with transient trapping and releasing functional DNA polymers via transient multivalency. CLSM measurements were conducted consecutively with the same microscopy settings. Scale bar, 10 μm.

(E) Time-dependent fluorescence intensities for the transient coacervates and entrapped fluorescent DNA polymers. Error bars are standard deviations from three random fields of view of duplicate experiments. Lines are guides to the eye.

(F) FI profiles for coacervates and entrapped functional DNA polymers at 4 h. Scale bar, 2 μm.

(G) Quantified FI ratios of the $FI_{periphery}$ to the FI_{center} of the coacervates.

(H) Schematic illustration of GOx and HRP encapsulation in the coacervates.

(I) Catalytic activity of the multienzyme complex inside the coacervates in comparison with free enzymes and enzymes on ECs, but without coacervates. Reactions monitored by absorbance at 414 nm. Error bars are standard deviations of duplicate measurements. Conditions for (A) 37°C, 0.01 mM M5, 0.012 mM M2, 0.01 mM M3, 0.012 mM M4, ca. 4.68–6.68 × 10^7 beads/mL, 0.92 WU/μL T4 DNA ligase, 1.0 U/μL BsaI, and 0.06 mM ATP, under orbital shaking at 80 rpm. Conditions for (B) 37°C, 0.01 mM M5, 0.012 mM M2, 0.01 mM M3, 0.012 mM M4, 0.92 WU/μL T4 DNA ligase, 1.0 U/μL BsaI, ca. inert functional polymers of 2 nM repeating units, and 0.06 mM ATP, under orbital shaking at 80 rpm. Conditions for (h): 37°C, 0.5 nM GOx on ECs, 0.5 nM HRP on ECs, 2 mM $ABTS^{2-}$, SfNAP1, and SfNAP2 of 0.008 mM repeating units, under orbital shaking at 97 rpm. After coacervating for 2 h, 1 mM glucose was added, and absorbance was measured at 414 nm.

Time-dependent CLSM images visualize the transient trapping and release of the Cy3-SfNAPs (Figure 5D). Both fluorescence channels show a transient increase of the intensities, yet there is some relevant delay for the Cy3/biotin-SfNAPs (Figure 5E). The uptake is slightly delayed due to the small quantity compared to the coacervate-forming SfNAPs. Additionally, CLSM shows a homogeneous distribution of the static Cy3-SfNAP polymers in the coacervates for the first 2 h. Yet, after 4 h, when degradation sets in, the Cy3-SfNAP is clearly more visible at the periphery of the coacervates (Figures 5F and 5G). This is because, when ATP is substantially consumed, there is a degradation of the SfNAP1 (bearing the same multivalent binder as the static Cy3/biotin-SfNAPs), and its decreased multivalent binding to the coacervates accumulates some Cy3/biotin-SfNAPs at the periphery of the coacervates.

One of the key aspects of LLPS is to provide spatially confined reaction compartments for catalysis with local enrichment and macromolecular crowding. To demonstrate a proof-of-concept catalytic reaction, we used the biotin motifs on the Cy3/biotin-SfNAPs to encapsulate streptavidin(StAv)-conjugated biomolecules, more precisely, StAv-based fusion proteins of GOx and HRP, which can form an enzymatic cascade (Figure S7; Note S1). In this enzyme cascade system, GOx first catalyzes oxidization of glucose, and the generated H_2O_2 is used by HRP to oxidize 2,2′-azino-bis(3-ethylbenzothiazoline-6-sulfonic acid) diammonium salt ($ABTS^{2-}$) into $ABTS^{-\cdot}$, which can be traced colorimetrically at 414 nm. Here, static coacervates were applied to investigate the catalytic efficacy of the enzyme cascade reaction of GOx and HRP in the macromolecularly crowded coacervate environment (Figure 5H). Non-fluorescent SfNAP1 and $ATTO_{647}$-SfNAP2 (8 μM for each species regarding amounts of repeating units) were mixed together with 0.5 nM GOx and HRP (separately pre-anchored to Cy3/biotin-SfNAPs), and 2 mM $ABTS^{2-}$. After a 2 h coacervation via orbital shaking at 97 rpm, 1 mM glucose was added, and the catalytic efficacy was monitored at 414 nm absorbance. We find a significantly increased catalytic efficiency for the enzyme cascade encapsulated in the DNA coacervates as compared to free enzymes or enzymes immobilized on the DNA polymers (EC; enzyme carrier; Figure 5I). This demonstrates, first of all, efficient diffusion of educts and products within the coacervates and, second, that the coacervates provide a propitious environment for the catalysis, which is due to molecular crowding and spatial proximity effect.[62] The results underscore the potential for using the multivalency guided all-DNA coacervates as reactors for versatile reactions.

DISCUSSION

We have demonstrated, for the first time, the multivalency-driven LLPS of two orthogonal SfNAPs for artificial membrane-less organelles, serving as a model

system to understand the multivalency-driven LLPS in biological systems. Fuel-driven coacervates have been realized by coupling the SfNAPs-forming building blocks to an ERN of ATP-powered ligation and BsaI-controlled restriction, rendering transient multivalency-driven all-DNA coacervates showing programmable lifetimes by ATP fuel level. By encoding molecular recognitions both in sticky ends and short side chains on various building blocks, we further demonstrated self-sorting of the LLPS for multicomponent coacervates in the same system, reminiscent of the diverse membrane-less organelles in biological systems.

Critically, the molecular recognition during LLPS allows for multivalent trapping of complementary ssDNA-functionalized objects, and the isothermal LLPS opens possibilities to encapsulate temperature-sensitive components, such as enzymes or proteins in general. We proved this by trapping micron-scale colloids for temporal formation of hybrid superstructures and trapping catalytically active biomolecules, GOx and HRP, for improved efficiency of the enzyme cascade.

Looking to the future, we foresee that this transient multivalency-driven LLPS provides completely new insights for significantly and swiftly advancing the fields of life-like materials, systems chemistry, and synthetic biology, as well as for better understanding of some principles of the dynamic structures in living systems. We believe that more external and autonomous control mechanisms can simply be encoded by providing light-switchable and reconfigurable components.[35,53,63] However, oscillatory behavior is hard to achieve in our coacervate system, as the reversible switches in the ERN cannot be as swift as the systems using photo-switchable chromophores. We envision, in particular, that the concept of transient multivalency-driven temporal coacervates will allow investigation of biocatalytic reactions inside the coacervates, dynamic condensation of proteins and nucleic acids for programmable biofunctions, and to program synthetic cells with hierarchical dynamic structures, enabling applications in biomedical engineering.

EXPERIMENTAL PROCEDURES

Resource Availability

Lead Contact

Further information and requests for resources should be directed to and will be fulfilled by the Lead Contact, Andreas Walther (andreas.walther@uni-mainz.de).

Materials Availability

This study did not generate any new unique reagents.

Data and Code Availability

This study did not generate or analyze any datasets or codes.

Syntheses of SfNAPs

dsDNA tiles M1 and M3 were first annealed from complementary ssDNA, D_1/D_2, and D_4/D_5, respectively (see sequences in Table S1). The syntheses of SfNAP1 and SfNAP2 followed with the same protocol. Briefly, the experiments were performed at 37°C in 1× *NEB* CutSmart buffer (50 mM potassium acetate, 20 mM tris-acetate, 10 mM magnesium acetate, and 100 μg/mL BSA) containing 0.02 mM M1 (or M3), 0.024 mM M2 (or M4), 0.46 Weiss Units (WU)/μL T4 DNA ligase, and 0.25 mM ATP, and the reactions were run for 12 h (the addition of a bit more tile M2 or M4 helps to suppress slight pipetting errors, ensuring efficient polymerizations). For analyses of the SfNAPs, 6 μL aliquots of the reaction solutions were quenched by 8 μL of the quenching buffer. Afterwards, all quenched samples were analyzed by AGE (2 wt

% agarose gel in TAE buffer) using 90 V for 2-h run time. The results were recorded by a transilluminator (UVsolo *touch* Gel electrophoresis documentation system, Analytik Jena).

LLPS of Two Orthogonal SfNAPs

The above obtained SfNAP1 and SfNAP2 solutions were mixed with equal volumes (60 μL in total) in a well of an imaging plate at 37°C under orbital shaking at 80 rpm. The temperature was controlled by a Hokai-Hit Stage Top Incubator System. The mixed solution was sealed with a layer of hexadecane (40 μL) to prevent evaporation. At different time intervals, CLSM was applied to characterize the coacervates formed through multivalency-driven LLPS. 63× water immersion objective was used throughout this study. CLSM measurements were conducted consecutively with the same microscopy settings. The DNA coacervates were quantified by ImageJ with regard to their size and fluorescent intensity over time. Briefly, the size and average fluorescent intensity of each individual coacervate were measured manually by line and circle selections, respectively. The line was drawn through the center of the coacervate, and the circle selection covered at least 80% of the area for the whole coacervate. Small and irregular aggregates with very faint fluorescence and less than 1 μm diameter were not counted. For the autonomous process below, the small coacervates with less than 1 μm diameter were also counted at 30 min due to their overall very small size.

ATP-fueled Transient Membrane-less All-DNA Coacervates

All the coacervation experiments for CLSM imaging were performed using 60 μL aqueous solutions sealed by 40 μL hexadecane. Typical experiments were conducted in 1× *NEB* CutSmart buffer at 37°C containing 0.01 mM M1, 0.012 mM M2, 0.01 mM M3, 0.012 mM M4, 0.92 WU/μL T4 DNA ligase, 1.0 U/μL BsaI as well as 0.06, 0.1, or 0.2 mM ATP, under orbital shaking at 80 rpm. The reaction solution was sealed in a well of an imaging plate by a layer of hexadecane. At different time intervals, CLSM was applied to monitor the DNA coacervates. It is worth noting that for the measurements at 30 min, the solutions were set still for ca. 5 min prior to the measurements to let the coacervates sediment a bit and facilitate the nucleation. For the AGE analyses of the time-dependent distributions of the SfNAPs, the experiments were performed with same conditions as above. At different time intervals, 6 μL aliquots of the reaction solutions were quenched by 8 μL of the quenching buffer and analyzed by AGE (see above). To investigate the effects of shaking on the coacervates, the experiments were conducted similar to the one mentioned above. Two groups of experiments were fueled with 0.06 mM ATP and performed under orbital shaking at 400 rpm and without shaking, respectively. CLSM was implemented to characterize the coacervates, and CLSM measurements were conducted consecutively with the same microscopy settings.

SUPPLEMENTAL INFORMATION

Supplemental Information can be found online at https://doi.org/10.1016/j.chempr.2020.09.022.

ACKNOWLEDGMENTS

We acknowledge support by the European Research Council starting grant (TimeProSAMat) Agreement 677960, as well as from the DFG Cluster of Excellence livMatS "Living, Adaptive and Energy-Autonomous Materials Systems", EXC-2193/1 - 390951807.

AUTHOR CONTRIBUTIONS

Conceptualization, J.D. and A.W.; Methodology, J.D. and A.W.; Investigation, J.D; Writing – Original Draft, J.D.; Writing – Review & Editing, J.D. and A.W.; Funding Acquisition, A.W.; Resources, A.W.; Supervision, A.W.

DECLARATION OF INTERESTS

The authors declare no competing interests.

Received: June 10, 2020
Revised: August 24, 2020
Accepted: September 23, 2020
Published: October 21, 2020

REFERENCES

1. Shin, Y., and Brangwynne, C.P. (2017). Liquid phase condensation in cell physiology and disease. Science *357*, eaaf4382.

2. Banani, S.F., Lee, H.O., Hyman, A.A., and Rosen, M.K. (2017). Biomolecular condensates: organizers of cellular biochemistry. Nat. Rev. Mol. Cell Biol. *18*, 285–298.

3. Case, L.B., Zhang, X., Ditlev, J.A., and Rosen, M.K. (2019). Stoichiometry controls activity of phase-separated clusters of actin signaling proteins. Science *363*, 1093–1097.

4. Li, X.H., Chavali, P.L., Pancsa, R., Chavali, S., and Babu, M.M. (2018). Function and regulation of phase-separated biological condensates. Biochemistry *57*, 2452–2461.

5. Strzyz, P. (2019). Phase separation tunes signal transduction. Nat. Rev. Mol. Cell Biol. *20*, 263.

6. Li, P., Banjade, S., Cheng, H.C., Kim, S., Chen, B., Guo, L., Llaguno, M., Hollingsworth, J.V., King, D.S., Banani, S.F., et al. (2012). Phase transitions in the assembly of multivalent signalling proteins. Nature *483*, 336–340.

7. Brangwynne, C.P., Eckmann, C.R., Courson, D.S., Rybarska, A., Hoege, C., Gharakhani, J., Jülicher, F., and Hyman, A.A. (2009). Germline P granules are liquid droplets that localize by controlled dissolution/condensation. Science *324*, 1729–1732.

8. Brangwynne, C.P., Mitchison, T.J., and Hyman, A.A. (2011). Active liquid-like behavior of nucleoli determines their size and shape in Xenopus laevis oocytes. Proc. Natl. Acad. Sci. USA *108*, 4334–4339.

9. Mao, Y.S., Zhang, B., and Spector, D.L. (2011). Biogenesis and function of nuclear bodies. Trends Genet *27*, 295–306.

10. Dundr, M. (2012). Nuclear bodies: multifunctional companions of the genome. Curr. Opin. Cell Biol. *24*, 415–422.

11. Nott, T.J., Petsalaki, E., Farber, P., Jervis, D., Fussner, E., Plochowietz, A., Craggs, T.D., Bazett-Jones, D.P., Pawson, T., Forman-Kay, J.D., and Baldwin, A.J. (2015). Phase transition of a disordered nuage protein generates environmentally responsive membraneless organelles. Mol. Cell *57*, 936–947.

12. Hernandez-Verdun, D. (2011). Assembly and disassembly of the nucleolus during the cell cycle. Nucleus *2*, 189–194.

13. Matera, A.G., Terns, R.M., and Terns, M.P. (2007). Non-coding RNAs: lessons from the small nuclear and small nucleolar RNAs. Nat. Rev. Mol. Cell Biol. *8*, 209–220.

14. Martin, N. (2019). Dynamic synthetic cells based on liquid–liquid phase separation. Chembiochem *20*, 2553–2568.

15. Dora Tang, T.Y., Rohaida Che Hak, C., Thompson, A.J., Kuimova, M.K., Williams, D.S., Perriman, A.W., and Mann, S. (2014). Fatty acid membrane assembly on coacervate microdroplets as a step towards a hybrid protocell model. Nat. Chem. *6*, 527–533.

16. Vieregg, J.R., Lueckheide, M., Marciel, A.B., Leon, L., Bologna, A.J., Rivera, J.R., and Tirrell, M.V. (2018). Oligonucleotide–peptide complexes: phase control by hybridization. J. Am. Chem. Soc. *140*, 1632–1638.

17. Adhikari, S., Prabhu, V.M., and Muthukumar, M. (2019). Lower critical solution temperature behavior in polyelectrolyte complex coacervates. Macromolecules *52*, 6998–7004.

18. Priftis, D., and Tirrell, M. (2012). Phase behaviour and complex coacervation of aqueous polypeptide solutions. Soft Matter *8*, 9396–9405.

19. Poudyal, R.R., Guth-Metzler, R.M., Veenis, A.J., Frankel, E.A., Keating, C.D., and Bevilacqua, P.C. (2019). Template-directed rna polymerization and enhanced ribozyme catalysis inside membraneless compartments formed by coacervates. Nat. Commun. *10*, 490.

20. Drobot, B., Iglesias-Artola, J.M., Le Vay, K., Mayr, V., Kar, M., Kreysing, M., Mutschler, H., and Tang, T.D. (2018). Compartmentalised RNA catalysis in membrane-free coacervate protocells. Nat. Commun. *9*, 3643.

21. Schoonen, L., and van Hest, J.C. (2016). Compartmentalization approaches in soft matter science: from nanoreactor development to organelle mimics. Adv. Mater. *28*, 1109–1128.

22. Li, J., Liu, X., Abdelmohsen, L.K.E.A., Williams, D.S., and Huang, X. (2019). Spatial organization in proteinaceous membrane-stabilized coacervate protocells. Small *15*, e1902893.

23. Mason, A.F., Buddingh', B.C., Williams, D.S., and van Hest, J.C.M. (2017). Hierarchical self-assembly of a copolymer-stabilized coacervate protocell. J. Am. Chem. Soc. *139*, 17309–17312.

24. Williams, D.S., Patil, A.J., and Mann, S. (2014). Spontaneous structuration in coacervate-based protocells by polyoxometalate-mediated membrane assembly. Small *10*, 1830–1840.

25. Deshpande, S., Brandenburg, F., Lau, A., Last, M.G.F., Spoelstra, W.K., Reese, L., Wunnava, S., Dogterom, M., and Dekker, C. (2019). Spatiotemporal control of coacervate formation within liposomes. Nat. Commun. *10*, 1800.

26. Chang, L.W., Lytle, T.K., Radhakrishna, M., Madinya, J.J., Vélez, J., Sing, C.E., and Perry, S.L. (2017). Sequence and entropy-based control of complex coacervates. Nat. Commun. *8*, 1273.

27. Black, K.A., Priftis, D., Perry, S.L., Yip, J., Byun, W.Y., and Tirrell, M. (2014). Protein encapsulation via polypeptide complex coacervation. ACS Macro Lett *3*, 1088–1091.

28. Priftis, D., Leon, L., Song, Z., Perry, S.L., Margossian, K.O., Tropnikova, A., Cheng, J., and Tirrell, M. (2015). Self-assembly of α-helical polypeptides driven by complex coacervation. Angew. Chem. Int. Ed. Engl. *54*, 11128–11132.

29. Fan, Y., Tang, S., Thomas, E.L., and Olsen, B.D. (2014). Responsive block copolymer photonics triggered by protein–polyelectrolyte coacervation. ACS Nano *8*, 11467–11473.

30. Jeon, O., Wolfson, D.W., and Alsberg, E. (2015). In-situ formation of growth-factor-loaded coacervate microparticle-embedded hydrogels for directing encapsulated stem cell fate. Adv. Mater. *27*, 2216–2223.

31. Cinar, H., Cinar, S., Chan, H.S., and Winter, R. (2018). Pressure-induced dissolution and reentrant formation of condensed, liquid–liquid phase-separated elastomeric α-elastin. Chemistry *24*, 8286–8291.

32. Yang, S., Li, B., Wu, C., Xu, W., Tu, M., Yan, Y., Huang, J., Drechsler, M., Granick, S., and Jiang,

L. (2019). Steering coacervation by a pair of broad-spectrum regulators. ACS Nano *13*, 2420–2426.

33. Schuster, B.S., Reed, E.H., Parthasarathy, R., Jahnke, C.N., Caldwell, R.M., Bermudez, J.G., Ramage, H., Good, M.C., and Hammer, D.A. (2018). Controllable protein phase separation and modular recruitment to form responsive membraneless organelles. Nat. Commun. *9*, 2985.

34. Martin, N., Douliez, J.P., Qiao, Y., Booth, R., Li, M., and Mann, S. (2018). Antagonistic chemical coupling in self-reconfigurable host-guest protocells. Nat. Commun. *9*, 3652.

35. Martin, N., Tian, L., Spencer, D., Coutable-Pennarun, A., Anderson, J.L.R., and Mann, S. (2019). Photoswitchable phase separation and oligonucleotide trafficking in DNA coacervate microdroplets. Angew. Chem. Int. Ed. Engl. *58*, 14594–14598.

36. Koga, S., Williams, D.S., Perriman, A.W., and Mann, S. (2011). Peptide–nucleotide microdroplets as a step Towards a membrane-free protocell model. Nat. Chem. *3*, 720–724.

37. Aumiller, W.M., Jr., and Keating, C.D. (2016). Phosphorylation-mediated rna/peptide complex coacervation as a model for intracellular liquid organelles. Nat. Chem. *8*, 129–137.

38. Nakashima, K.K., Baaij, J.F., and Spruijt, E. (2018). Reversible generation of coacervate droplets in an enzymatic network. Soft Matter *14*, 361–367.

39. Te Brinke, E., Groen, J., Herrmann, A., Heus, H.A., Rivas, G., Spruijt, E., and Huck, W.T.S. (2018). Dissipative adaptation in driven self-assembly leading to self-dividing fibrils. Nat. Nanotechnol. *13*, 849–855.

40. Rieß, B., Grötsch, R.K., and Boekhoven, J. (2020). The design of dissipative molecular assemblies driven by chemical reaction cycles. Chem *6*, 552–578.

41. Deng, J., and Walther, A. (2020). ATP-responsive and ATP-fueled self-assembling systems and materials. Adv. Mater. https://doi.org/10.1002/adma.202002629.

42. Sun, M., Deng, J., and Walther, A. (2020). Polymer transformers: interdigitating reaction networks of fueled monomer species to reconfigure functional polymer states. Angew. Chem. Int. Ed. Engl. *59*, 18161–18165.

43. Zhang, D.Y., and Seelig, G. (2011). Dynamic DNA nanotechnology using strand-displacement reactions. Nat. Chem. *3*, 103–113.

44. Qian, L., and Winfree, E. (2011). Scaling up digital circuit computation with DNA strand displacement cascades. Science *332*, 1196–1201.

45. Song, T., Shah, S., Bui, H., Garg, S., Eshra, A., Fu, D., Yang, M., Mokhtar, R., and Reif, J. (2019). Programming DNA-based biomolecular reaction networks on cancer cell membranes. J. Am. Chem. Soc. *141*, 16539–16543.

46. Kim, Y.Y., Bang, Y., Lee, A.H., and Song, Y.K. (2019). Multivalent Traptavidin–DNA conjugates for the programmable assembly of nanostructures. ACS Nano *13*, 1183–1194.

47. Sato, Y., Sakamoto, T., and Takinoue, M. (2020). Sequence-based engineering of dynamic functions of micrometer-sized DNA droplets. Sci. Adv. *6*, eaba3471.

48. Nguyen, D.T., Jeon, B.J., Abraham, G.R., and Saleh, O.A. (2019). Length-dependence and spatial structure of DNA partitioning into a DNA liquid. Langmuir *35*, 14849–14854.

49. Jeon, B.J., Nguyen, D.T., Abraham, G.R., Conrad, N., Fygenson, D.K., and Saleh, O.A. (2018). Salt-dependent properties of a coacervate-like, self-assembled DNA liquid. Soft Matter *14*, 7009–7015.

50. Zeng, J., Fu, W., Qi, Z., Zhu, Q., He, H., Huang, C., Zuo, H., and Mao, C. (2019). Self-assembly of microparticles by supramolecular homopolymerization of one component DNA molecule. Small *15*, e1805552.

51. Merindol, R., Loescher, S., Samanta, A., and Walther, A. (2018). Pathway-controlled formation of mesostructured all-DNA colloids and superstructures. Nat. Nanotechnol. *13*, 730–738.

52. Heinen, L., and Walther, A. (2019). Programmable dynamic steady states in Atp-driven nonequilibrium DNA systems. Sci. Adv. *5*, eaaw0590.

53. Deng, J., and Walther, A. (2020). Pathway complexity in fuel-driven DNA nanostructures with autonomous reconfiguration of multiple dynamic steady states. J. Am. Chem. Soc. *142*, 685–689.

54. Deng, J., and Walther, A. (2020). ATP-powered molecular recognition to engineer transient multivalency and self-sorting 4d hierarchical systems. Nat. Commun. *11*, 3658.

55. Dickson, K.S., Burns, C.M., and Richardson, J.P. (2000). Determination of the free-energy change for repair of a DNA phosphodiester bond. J. Biol. Chem. *275*, 15828–15831.

56. Ge, H., and Qian, H. (2013). Dissipation, generalized free energy, and a self-consistent nonequilibrium thermodynamics of chemically driven open subsystems. Phys Rev E Stat Nonlin Soft Matter Phys *87*, 062125.

57. Qian, H. (2006). Open-system nonequilibrium steady state: statistical thermodynamics, fluctuations, and chemical oscillations. J. Phys. Chem. B *110*, 15063–15074.

58. Qian, H., Kjelstrup, S., Kolomeisky, A.B., and Bedeaux, D. (2016). Entropy production in mesoscopic stochastic thermodynamics: nonequilibrium kinetic cycles driven by chemical potentials, temperatures, and mechanical forces. J. Phys. Condens. Matter *28*, 153004.

59. Qian, H., and Roy, S. (2012). An information theoretical analysis of kinase activated phosphorylation dephosphorylation cycle. IEEE Trans. Nanobiosci. *11*, 289–295.

60. Qian, H., and Bishop, L.M. (2010). The chemical master equation approach to nonequilibrium steady-state of open biochemical systems: linear single-molecule enzyme kinetics and nonlinear biochemical reaction networks. Int. J. Mol. Sci. *11*, 3472–3500.

61. Walther, A. (2019). From responsive to adaptive and interactive materials and materials systems: A roadmap. Adv. Mater. *32*, e1905111.

62. Ellis, R.J. (2001). Macromolecular crowding: obvious but underappreciated. Trends Biochem. Sci. *26*, 597–604.

63. Deng, J., Bezold, D., Jessen, H.J., and Walther, A. (2020). Multiple light control mechanisms in ATP-fueled non-equilibrium DNA systems. Angew. Chem. Int. Ed. Engl. *59*, 12084–12092.

Chem, Volume *6*

Supplemental Information

Programmable ATP-Fueled DNA Coacervates by Transient Liquid-Liquid Phase Separation

Jie Deng and Andreas Walther

Table of Contents

1. Materials and methods

1.1 Instrumentation

ThermoMixer (Eppendorf), UVsolo *touch* Gel electrophoresis documentation system (Analytik Jena), gel electrophoresis chambers (biostep), power source 250 V (VWR), Image J, ScanDropR UV-VIS spectrometer (Analytik Jena), Confocal laser scanning microscopy (Leica TCS SP8, Mannheim), STX Stage Top Incubator System (Tokai Hit, Japan), and Spark® Multimode Microplate Reader (Tecan).

1.2 Reagents and materials

T4 DNA ligase (HC, 20 WU/µL, recombinant *E. coli* strain) was supplied by Promega and BsaI-HF®v2 (20 units/µL, *NEB #R3733*) was ordered from New England Biolabs (*NEB*). ATP solution (10 mM in 1 mM Tris-HCl pH 7.5) was purchased from Invitrogen. Agarose low EEO was supplied by PanReac AppliChem. Gene ruler 1k bp and 50 bp DNA ladders (ready to use), DNA gel loading dye (6×), horseradish peroxidase-conjugated streptavidin (N100), and streptavidin coated magnetic microparticles (Dynabeads™ MyOne™ Streptavidin C1) were supplied by ThermoFisher Scientific. Streptavidin-glucose oxidase was ordered from Fitzgerald (65R-S124). Ethylenediaminetetraacetic acid disodium salt dihydrate (EDTA, biology grade) was supplied by CALBIOCHEM. Sodium chloride (NaCl, 99%), hexadecane (99%), tris (hydroxymethyl)aminomethane hydrochloride pH 8.0 (Tris-HCl), trizma base, D-glucose (> 99.5%), and 2,2′-azino-bis(3-ethylbenzothiazoline-6-sulfonic acid) diammonium salt ($ABTS^{2-}$, > 98%) were ordered from Sigma-Aldrich. Acetic acid glacial (ACS, Reag. Ph. Eur. Analytical reagents) was supplied by VWR Chemicals. RotiR-GelStain (1,1'3,3',5,5'6,6'-octamethyl-2,2'-spiro(2,3-dihydro-1H-benzimidazol) was supplied by Carl Roth. All oligonucleotides were supplied by Integrated DNA Technologies Inc.. Corning® high content imaging plates (96 wells, black wells (with 0.2 mm glass bottom), half area) were supplied by Sigma-Aldrich.

Buffer compositions

T4 DNA Ligase Storage Buffer (Promega): 10 mM Tris-HCl (pH 7.4 at 25 °C), 50 mM KCl, 1 mM dithiothreitol (DTT), 0.1 mM EDTA, 50% glycerol.

BsaI-HF®v2 storage buffer (NEB): 10 mM Tris-HCl, 200 mM NaCl, 1 mM DTT, 0.1 mM EDTA, 200 µg/mL BSA, 50% glycerol.

NEB CutSmart® Buffer: 50 mM potassium acetate, 20 mM Tris-acetate, 10 mM magnesium acetate, 100 µg/mLBSA.

Annealing Buffer: 10 mM Tris-HCl (pH 8.0), 50 mM NaCl.

TAE Buffer: 40 mM Tris, 20 mM acetic ccid, 1 mM EDTA.

Quenching Buffer: 200 mM EDTA, 10 mM Tris-HCl (pH 8.0), 50 mM NaCl.

CSF buffer: *CutSmart® Buffer* supplemented with 0.05% Pluronic® F-127.

Milli-Q water was used throughout of this study.

Supplementary Table 1: Oligonucleotide sequences used, with their name in individual Figure, the sequence codes used for ordering at IDT, and their ID in experimental section.

Name	Oligonucleotide sequence (5'-3')	Purification	ID
M1	/5Phos/GATTAGAGACCGTACCTACATATAGCTACTG ATACTCT	HPLC	D_1
	/5ATTO488N/AGCTATATGTAGGTACGGTCTCT	HPLC	D_2
M2	/5Phos/AATCAGAGTATCTTTTTCGAATAGAGG	HPLC	D_3
M3	/5Phos/ATGAAGAGACCGTACCTACATATAGCTACTA CTTGATA	HPLC	D_4
	/5ATTO647NN/AGCTATATGTAGGTACGGTCTCT	HPLC	D_5
M4	/5Phos/TCATTATCAAGTTTT TTCCTCTATTCG	HPLC	D_6
M5	/5Phos/GATTAGAGACCGTACCTACATATAGCTACTG ATACTCT	HPLC	D_1
	AGCTATATGTAGGTACGGTCTCT	HPLC	D_7
DoS	CATAGGTAGAAGTGT/3ATTO488N/	HPLC	D_8
	/5BiosG/ACACTTCTACCTATGTTTTTTTTCACCTCTAT TCG	Desalting	D_9
$2/3M_{EC}$	/5Phos/GTCAAGATATCGTACCTACATATAGTCACTTC AATAGC	HPLC	D_{10}
	/5BiosG/GAGTATATGTAGGTACGATATCT	HPLC	D_{11}
$1/3M_{EC}$	/5Phos/TGACGCTATTGATTTTTCCTCTATTCG/3Cy3Sp/	HPLC	D_{12}
M6	/5Phos/GTCAAG AGA CCG TAC CTA CAT ATA GCT ACT CAT TCC AA	HPLC	D_{13}
	/5ATTO488N/AGC TAT ATG TAG GTA CGG TCT CT	HPLC	D_{14}
M7	/5Phos/TGACTTGGAATGTTT TTC TCA TAC T	HPLC	D_{15}
M8	/5Phos/CTTAAG AGA CCG TAC CTA CAT ATA GCT ACT CCT ATG TG	HPLC	D_{16}
	AGCTATATGTAGGTACGGTCTCT	HPLC	D_7

M9	/5Phos/TAAGCACATAGGTTTTTAGTATGAG	HPLC	D_{17}

2. Experimental Protocols

2.1 Hybridization of the double-stranded DNA (dsDNA) tiles

All DNA strands were used as received, to which certain amounts of annealing buffer were added to make stock solutions and the concentrations were calculated via UV-VIS spectroscopy. The dsDNA tiles in this study were annealed from two complementary single-stranded (ssDNA) with the same stoichiometry at room temperature overnight. The annealed stock solutions (ca. 0.5 mM) were stored at -20 °C for further use.

2.2 Coacervates fusion

Typical experiments were conducted in 1× *NEB* CutSmart buffer at 37°C containing 0.01 mM M1, 0.012 mM M2, 0.01 mM M3, 0.012 mM M4, 0.92 WU/μL T4 DNA ligase, 1.0 U/μL BsaI as well as 0.2 mM ATP without shaking. The reaction solution was sealed in a well of an imaging plate by a layer of hexadecane. After reacting for 2 h, time-dependent measurements of the coacervates fusion were carried out under CLSM by time-lapse imaging in 2 min intervals over 5 h (Results in Figure S5 and Supplementary Video 1).

2.3 New DNA tile integration and dynamization in a running transient coacervates system

The experiments were performed in 1× *NEB* CutSmart buffer at 37°C containing 0.01 mM M5, 0.012 mM M2, 0.01 mM M3, 0.012 mM M4, 0.92 WU/μL T4 DNA ligase, 1.0 U/μL BsaI, and 0.2 mM of ATP, under orbital shaking at 80 rpm, followed by addition of another 0.002 mM M1 and 0.0024 mM M2 after 2 h running of the transient coacervation reaction. CLSM was implemented to characterize the coacervates at different time intervals, and the CLSM measurements were conducted consecutively with the same microscopy settings.

2.4 ATP-driven sorted LLPS for multicomponent coacervates

Typical experiments were performed in 1× *NEB* CutSmart buffer at 37°C containing 0.01 mM M5, 0.012 mM M2, 0.01 mM M3, 0.012 mM M4, 0.01 mM M6, 0.012 mM M7, 0.01 mM M8, 0.012 mM M9, 0.92 WU/μL T4 DNA ligase, 1.0 U/μL BsaI, and 0.12 mM ATP, under orbital shaking at 80 rpm. At different time intervals, CLSM was used to characterize the multicomponent coacervates, and the CLSM measurements were conducted consecutively with the same microscopy settings.

2.5 Immobilization of the docking strand on streptavidin-coated magnetic colloids

10 μL of streptavidin-coated magnetic particles (Dynabeads™ MyOne™ Streptavidin C1, ThermoFisher Scientific) were washed with 10 μL CSF buffer for 3 times. Afterwards, the particles were re-suspended in 20 μL CSF buffer with 0.05 mM docking strand (DoS, D_8/D_9) and the reaction was carried out at room temperature for 1 h. The particles were then washed by 10 μL CSF buffer 5 times, re-suspended in 10 μL CSF buffer, and stored in the refrigerator for further use.

2.6 ATP-driven transient colloids trapping and releasing in the DNA coacervates

The experiments were performed in 1× *NEB* CutSmart buffer at 37°C containing 0.01 mM M5, 0.012 mM M2, 0.01 mM M3, 0.012 mM M4, 0.92 WU/μL T4 DNA ligase, 1.0 U/μL BsaI, ca. 66.8 μg/mL DoS-modified colloids (ca. 4.68-6.68×10^7 beads/mL) as well as 0.06 mM ATP, under orbital shaking at 80 rpm. The reaction solution was sealed in a well of an imaging plate by a layer of hexadecane. At different time intervals, CLSM was applied to characterize transient colloid assembly and superstructure. CLSM measurements were conducted consecutively with the same microscopy settings. For another experiment, lower amount of colloids was used to control the structure of the assemblies. The experiments were performed at the same conditions as above but only 10 % of the colloids were used.

2.7 Synthesis of enzyme carrier (biotin modified BsaI-inert SfNAP)

The experiments were performed in 1× *NEB* CutSmart buffer at 37°C containing 0.05 mM 2/3M_{EC} (D_{10}/D_{11}), 0.06 mM 1/3M_{EC} (D_{12}), 0.92 WU/μL T4 DNA ligase, and 0.6 mM ATP for 12 h. Afterwards, the remaining ATP was removed by spin filtration washed by annealing buffer with 3 k molecular weight cut-off. The concentration of the products in terms of the amount of repeating units was calculated by the absorbance of Cy3 dye at 550 nm to be 0.04 mM. The obtained solution was stored in the refrigerator for further use.

2.8 ATP-driven transient trapping of the BsaI-inert SfNAP in DNA coacervates

The experiments were performed in 1× *NEB* CutSmart buffer at 37°C containing 0.01 mM M5, 0.012 mM M2, 0.01 mM M3, 0.012 mM M4, 0.92 WU/μL T4 DNA ligase, 1.0 U/μL BsaI, inert SfNAPs of 2 nM repeating units as well as 0.06 mM ATP, under orbital shaking at 80 rpm. The reaction solution was sealed in a well of an imaging plate by a layer of hexadecane. At different time intervals, CLSM was applied to characterize transient polymer trapping and releasing.

2.9 Immobilization of glucose oxidase (GOx) and horseradish peroxidase (HRP) to enzyme carrier

100 nM streptavidin-GOx (or streptavidin-HRP) was mixed with enzyme carrier (containing 100 nM biotin) in 1× *NEB* CutSmart buffer, and the conjugation reaction was performed at a refrigerator for overnight. The obtained products were immediately used for further experiments.

2.10 ATP-driven transient enzymes encapsulation

The experiments were performed in 1× *NEB* CutSmart buffer at 37°C containing 0.01 mM M5, 0.012 mM M2, 0.01 mM M3, 0.012 mM M4, 0.92 WU/μL T4 DNA ligase, 1.33 U/μL BsaI, 0.5 nM GOx on enzyme carriers, 0.5 nM HRP on enzyme carriers, and 0.06 mM ATP, under orbital shaking at 80 rpm. The reaction solution was sealed in a well of an imaging plate by a layer of hexadecane. At different time intervals, CLSM was applied to characterize the coacervates, and the CLSM measurements were conducted consecutively with the same microscopy settings.

2.11 Multienzyme cascades in membrane-less all-DNA coacervates

The experiments were performed in 1× *NEB* CutSmart buffer at 37°C containing 0.5 nM GOx on enzyme carriers, 0.5 nM HRP on enzyme carrier, 2 mM $ABTS^{2-}$, SfNAP1 and SfNAP2 of 0.008 mM repeating units, under orbital shaking at 96 rpm (due to the lower limit of the plate

reader). After coacervating for 2 h, 1 mM glucose was added to trigger the multienzyme cascades, and the catalytic efficacy was monitored by a plate reader via absorbance at 414 nm. Control experiments were conducted by free enzymes or enzymes on the enzyme carriers but without coacervates at the same conditions as above.

3. Supplementary Figures

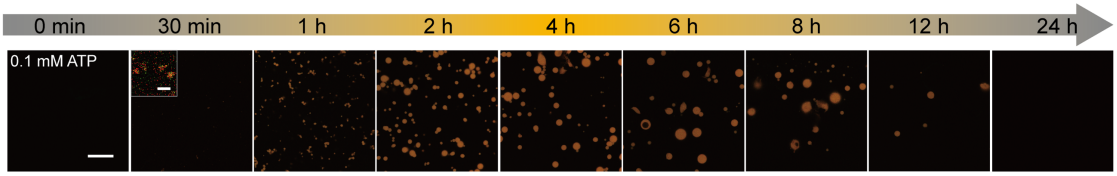

Figure S1. ATP-driven transient all-DNA coacervates. Time-dependent CLSM measurements of transient all-DNA coacervates fueled by 0.1 mM ATP. CLSM measurements were conducted consecutively with the same microscopy settings. Scale bar = 20 μm; insert = 2 μm.

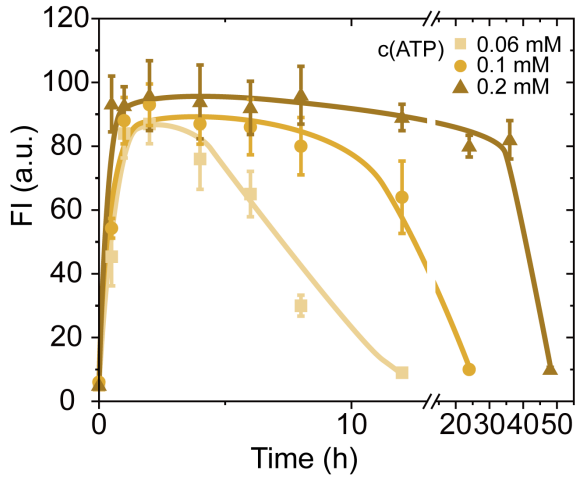

Figure S2. Time-dependent fluorescence intensity of the transient coacervates fueled with 0.06, 0.1, and 0.2 mM ATP. Error bars are standard deviations from three random fields of view of duplicate experiments. Ca. 300 coacervates were counted at the dynamic steady state, while 10-50 coacervates were counted at the degradation stage due to significantly decreased number of coacervates. Lines are guides to the eye.

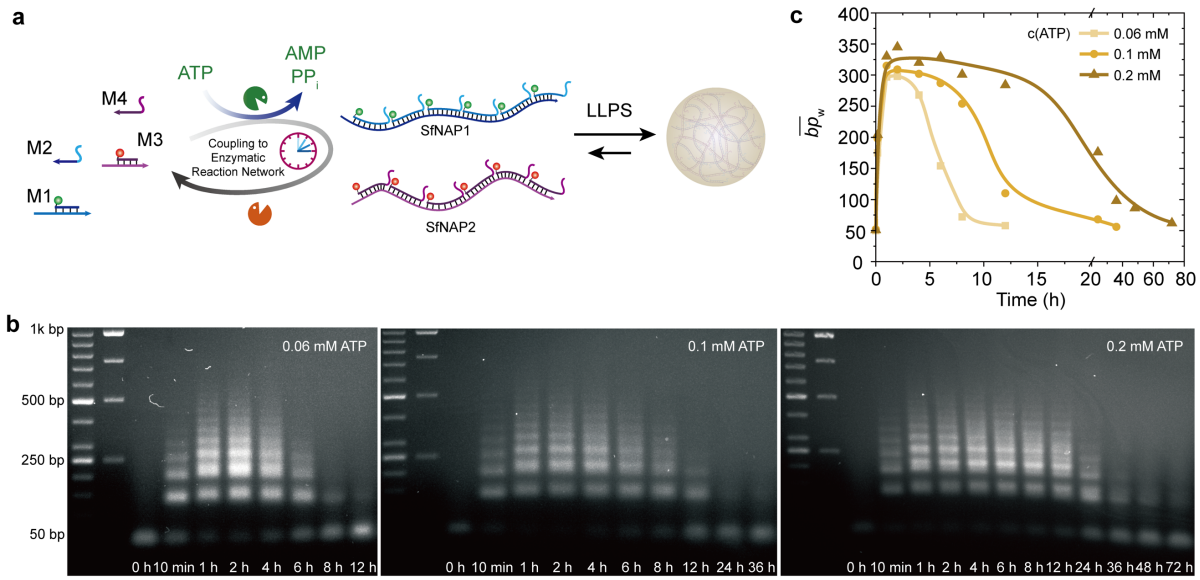

Figure S3. Analyses of the transient SfNAPs in the transient DNA coacervates. (**a**) Schematic representation of ATP-driven transient coacervates by LLPS of transient SfNAPs. (**b**) Time-dependent AGE (2 wt. %, 90 V, 2 h) for transient DNA polymerizations with programmable lifetimes by fueling with varied ATP concentration (0.06, 0.1, and 0.2 mM). (**c**) The mass-weighted average chain length ($\overline{bp_w}$) development with time by varying the ATP concentration from 0.06 to 0.2 mM. Lines are guides to the eye. Conditions: 37°C, 0.01 mM M1, 0.012 mM M2, 0.01 mM M3, 0.012 mM M4, 0.92 WU/µL T4 DNA ligase, 1.0 U/µL BsaI, and varying amounts of ATP, under orbital shaking at 80 rpm.

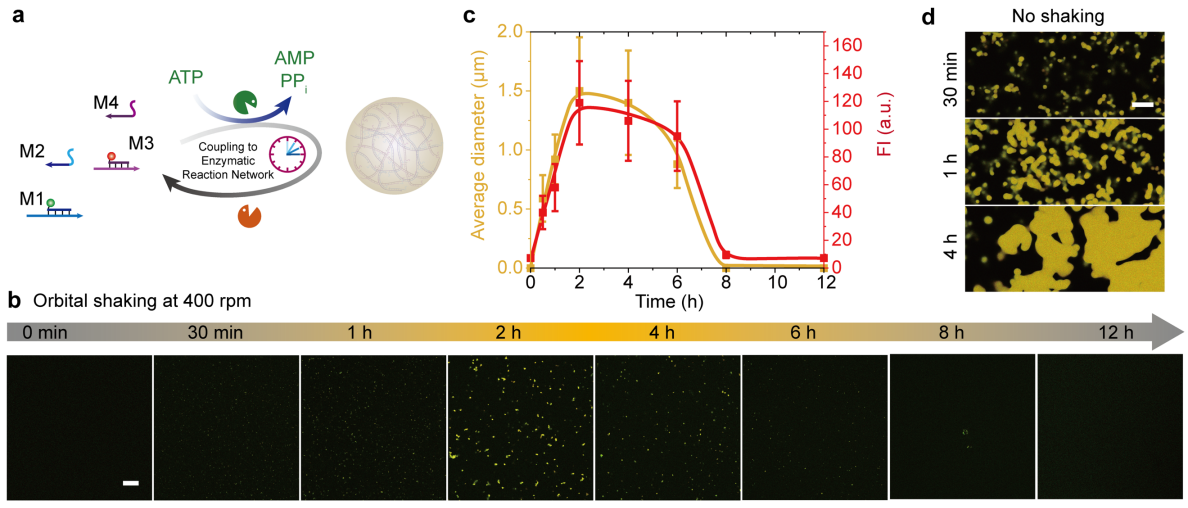

Figure S4. Mechanical responsiveness of the transient DNA coacervates. (**a**) Schematic illustration of ATP-driven transient DNA coacervates. (**b**) Time-dependent CLSM measurements of the coacervates under orbital shaking at 400 rpm. Scale bar = 20 µm. (**c**) Time-dependent average diameter and fluorescence intensity ($ATTO_{647}$) for the coacervates. Error bars are standard deviations from three random fields of view of duplicate experiments. Lines are guides to the eye. (**d**) CLSM measurements of the coacervates with time for the experiment

without shaking. Scale bar = 20 µm. Conditions: 37°C, 0.01 mM M1, 0.012 mM M2, 0.01 mM M3, 0.012 mM M4, 0.92 WU/µL T4 DNA ligase, 1.0 U/µL BsaI, and 0.06 mM ATP, under orbital shaking at (**b**) 400 and (**d**) 0 rpm.

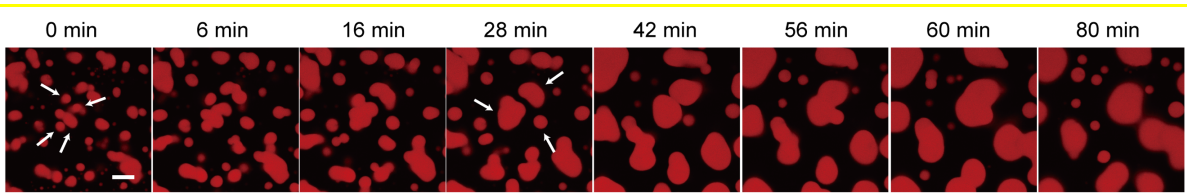

Figure S5. Coacervate fusion. Time-dependent CLSM measurements during fusion of the ATP-fueled DNA coacervates by removing shaking for maturation. Measurements were carried out 2 h after adding ATP. Scale bar = 10 µm. Conditions: 37°C, 0.01 mM M1, 0.012 mM M2, 0.01 mM M3, 0.012 mM M4, 0.92 WU/µL T4 DNA ligase, 1.0 U/µL BsaI, and 0.2 mM ATP, without shaking.

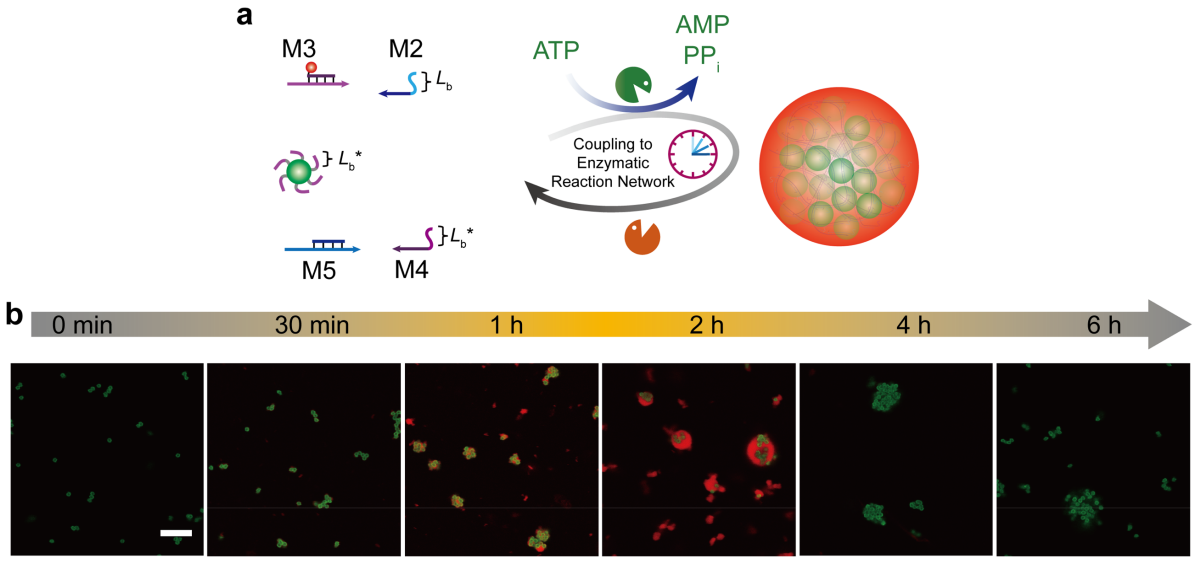

Figure S6. Transient trapping and releasing of colloids using 10 % colloids as in Figure 5c in main manuscript. (**a**) Schematic illustration of ATP-driven transient coacervates for temporal trapping micron-sized colloids. (**b**) Time-dependent CLSM measurements of the transient superstructures. Scale bar = 10 µm. Conditions: 37°C, 0.01 mM M5, 0.012 mM M2, 0.01 mM M3, 0.012 mM M4, 0.92 WU/µL T4 DNA ligase, 1.0 U/µL BsaI, ca. 6.68 µg/mL DoS-modified colloids (ca. 4.68-6.68×10^6 beads/mL) as well as 0.06 mM ATP, under orbital shaking at 80 rpm.

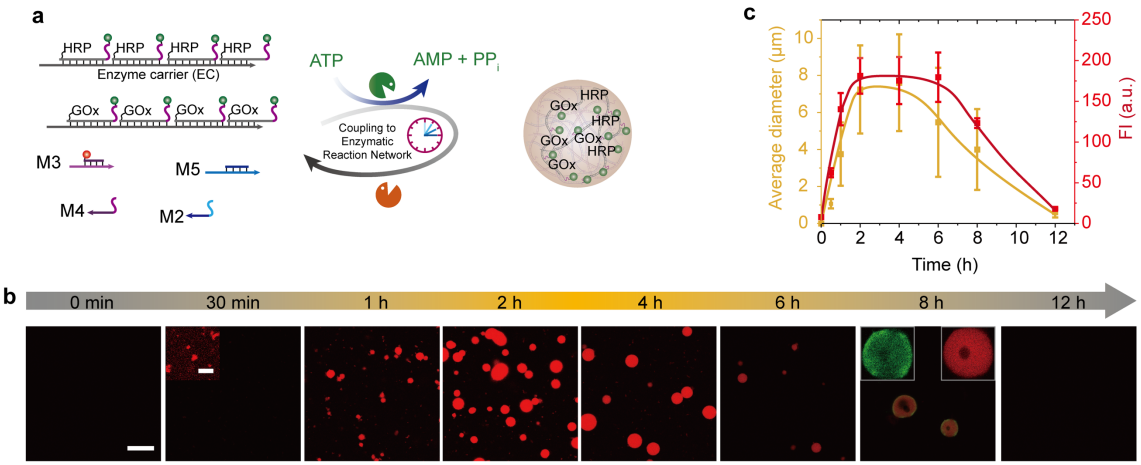

Figure S7. ATP-driven transient trapping and releasing of multienzyme complex. (**a**) Schematic illustration of ATP-driven transient encapsulation of GOx and HRP. (**b**) Time-dependent CLSM measurements of enzymes loaded coacervates. Scale bar = 20 μm; insert = 4 μm. (**c**) Average diameters and fluorescence intensities for the coacervates over time. Error bars are standard deviations from three random fields of view of duplicate experiments. Lines are guides to the eye. Conditions: 37°C, 0.01 mM M5, 0.012 mM M2, 0.01 mM M3, 0.012 mM M4, 0.92 WU/μL T4 DNA ligase, 1.33 U/μL BsaI, 0.5 nM GOx on enzyme carriers, 0.5 nM HRP on enzyme carriers, and 0.06 mM ATP, under orbital shaking at 80 rpm.

Supplementary Note 1. ATP-driven transient trapping of multienzyme complex

For proof-of-concept, we conjugated GOx and HRP to the biotin functionalized DNA polymer, enzyme carrier (EC), for transient biomolecules encapsulation in the transient coacervates. Upon running the GOx and HRP immobilized functional DNA polymers with the transient coacervate system, transient encapsulation of multienzyme complex is achieved (Figure S7b). However, the multienzyme complex shows significant inhibition on BsaI. Thus, compared to the system above without multienzyme complex, the degradation of the coacervates with multienzyme complex is more time-consuming and more restriction enzyme is needed for successful coacervates degradation. In principle, the biomolecules could be any other streptavidin, neutravidin or avidin conjugated biomolecules, and the conjugation interaction between the DNA and the biomolecules can also be changed to some other interactions, such as His-tag or click chemistry. Hence, our strategy provides a universal method to encapsulate biomolecules inside the coacervates for versatile functions.